GEOPHYSICS, VOL. 87, NO. 2 (MARCH-APRIL 2022); P. U29–U41, 15 FIGS.
10.1190/GEO2021-0116.1

Topography-dependent eikonal tomography based on the fast-sweeping scheme and the adjoint-state technique

Gaoshan Guo[1], Haiqiang Lan[1], Xiaole Zhou[1], Youshan Liu[1], Umair Bin Waheed[2], and Jingyi Chen[3]

ABSTRACT

First-arrival traveltime tomography has been widely used for upper crustal velocity modeling, but it usually suffers from the problem of complex surface topography. To overcome this problem, we have developed a new topography-dependent eikonal tomography scheme that combines a developed accurate and efficient traveltime modeling method and introduces a flexible and robust adjoint inversion scheme in the presence of irregular topography. A surface-flattening scheme is used to handle the irregular surface, where the real model is discretized by curvilinear grids and the irregular free surface is mathematically flattened through the transformation from Cartesian to curvilinear coordinates. Based on this parameterization, the forward traveltime modeling is conducted by a monotone fast-sweeping method that discretizes the factored topography-dependent eikonal equation with a point-source condition. This algorithm can circumvent the source-singularity problem and decrease the numerical error in the vicinity of a point source in the curvilinear system. Then, the gradient-based inversion is used to minimize the misfit function, which is achieved by a matrix-free adjoint-state method without cumbersome ray tracing and explicit estimation of the Fréchet derivative matrix in the curvilinear coordinate system. The new tomographic scheme is evaluated through numerical examples with different seismic structures with complex topography, and then applied to a wide-angle profile acquired in the northeastern Tibetan Plateau. The results validate the effectiveness and efficiency of our tomography scheme in constructing shallow crustal velocity models with irregular topography.

INTRODUCTION

The seismic structure of the earth's crust has been extensively investigated by traveltime tomography, a technique widely used in natural resource prospecting and exploration of the earth's interior during past decades (Aki et al., 1977; Korenaga et al., 2000; Roecker et al., 2006; Rawlinson and Kennett, 2008; Koulakov, 2009; Huang and Bellefleur, 2011; Zhou et al., 2019). Traveltime tomography is usually based on ray-tracing methods (Thurber, 1983; Zhao et al., 1992; Xu et al., 2006; Zhou and Greenhalgh, 2008) or grid-based schemes (Vidale, 1988; Sethian and Popovici, 1999; Rawlinson and Sambridge, 2004; Zhao, 2005; Han et al., 2017). Grid-based solvers have proven to be considerably faster than classic ray-tracing methods when many source-receiver couples are considered. Problems such as shadow zones, multipathing, and barrier penetration, which are common in ray-tracing methods, also can be easily handled by grid-based solvers. However, most of the available grid-based traveltime tomography schemes have difficulty dealing with irregular topography.

In practice, an irregular free surface is a common situation in seismic exploration, which makes the reconstruction of subsurface structures rather difficult in oil/gas reservoir surveys and deep seismic soundings (Reshef, 1991; Rajasekaran and McMechan, 1995; Knapp et al., 2004). To date, several methods based on unstructured

Manuscript received by the Editor 28 February 2021; revised manuscript received 27 September 2021; published ahead of production 2 November 2021; published online 27 December 2021.
[1]Chinese Academy of Sciences, State Key Laboratory of Lithospheric Evolution, Institute of Geology and Geophysics, Beijing 100029, China and University of Chinese Academy of Sciences, Beijing 100049, China. E-mail: guogs@mail.iggcas.ac.cn; lanhq@mail.iggcas.ac.cn (corresponding author); zhouxiaole@mail.iggcas.ac.cn; ysliu@mail.iggcas.ac.cn.
[2]King Fahd University of Petroleum and Minerals, College of Petroleum Engineering and Geosciences, Dhahran 31261, Saudi Arabia. E-mail: umairbin.waheed@kaust.edu.sa.
[3]The University of Tulsa, Department of Geosciences, Tulsa, Oklahoma 74104-9700, USA. E-mail: jingyi-chen@utulsa.edu.

grids have been proposed to overcome this problem (Zhang and Thurber, 2005; Lelièvre et al., 2011; Salcedo et al., 2020). Although the traveltime inversion on unstructured grids could exactly describe the complex topography, they usually involve troublesome parameterization, complex and time-consuming eikonal solvers, and inversion schemes. However, the model discretization and forward-modeling scheme based on structured grids often are more convenient and straightforward, thus making the inversion on these grids more feasible and useful for practical applications (Hole, 1992; Zhang et al., 1998; Huang and Bellefleur, 2012; Ma and Zhang, 2015).

In view of this, a model expansion technique is sometimes adopted to deal with irregular topography. But recent studies demonstrate that the transition from an irregular free surface to an inner discontinuity using a model expansion scheme may cause problems, such as physically unrealistic seismic raypaths and spurious ray take-off angles (Ma and Zhang, 2015; Zhang et al., 2017; Guo et al., 2019). To overcome these undesirable problems, Ma and Zhang (2015) develop an alternative tomographic method making use of the topography-dependent eikonal equation (TDEE) (Lan and Zhang, 2013a, 2013b) and the back-projection inversion algorithm (Hole, 1992). In this scheme, the irregular topographic surface of the real model is mathematically flattened and preserved as a free surface, as shown in Figure 1. However, in this approach, the Lax-Friedrichs sweeping scheme used for approximating the viscosity solution of TDEE (Lan and Zhang, 2013a, 2013b) is dissipative and needs a much larger number of iterations to converge. Moreover, the back-projection inversion suffers from stability and convergence problems and does not lend itself naturally to regularization (Rawlinson et al., 2010).

During inversion, the raypath is traced and approximated by a series of ray segments in the computational grids (Hole, 1992), which is highly complicated and unstable, especially in the curvilinear coordinate system (Ma and Zhang, 2015). To overcome these difficulties, we introduce the new matrix-free gradient-based first-arrival traveltime tomography method in curvilinear coordinates. The first key ingredient is the computation of traveltimes by solving the factored TDEE (FTDEE) with a fast-sweeping method (Fomel et al., 2009; Luo and Qian, 2012; Huang et al., 2020; Zhou et al., 2020). This new monotone method converges after a finite number of iterations, independent of the mesh size, which makes it an efficient and robust tool for calculating traveltimes in the presence of an irregular free surface. Moreover, a factored form of TDEE can capture source singularity and significantly improve the accuracy of the solution, especially for areas around the source (Zhou et al., 2020). The second key ingredient is the efficient computation of the gradient of the misfit function with respect to model parameters by a matrix-free adjoint-state method (Sei and Symes, 1994; Leung and Qian, 2006; Taillandier et al., 2009; Noble et al., 2010; Benaichouche et al., 2015; Waheed et al., 2016; Li et al., 2017; Tavakoli et al., 2017; Sambolian et al., 2019) to avoid computation and storage of Fréchet derivatives using intricate and unstable posterior ray tracing in the curvilinear coordinate system (Ma and Zhang, 2015). In addition, the cost of computing the gradient of the objective function using the adjoint-state method is only twice the cost of the forward problem. The amount of memory required is governed by the size of the discretized model space and is independent of the available data. These computational advantages make the adjoint-state method promising for large-scale data sets.

In the following, we introduce the factorized TDEE solver used for traveltime modeling. Then, the theory of the adjoint-state inversion method in a curvilinear coordinate system, mainly developed in this study, is presented. Next, we show a simple velocity model with complex topography to illustrate the calculation of the gradient. Later, several different numerical examples are shown to evaluate the feasibility and accuracy of the method through synthetic traveltime data sets and a field data set acquired in northeastern Tibet. Finally, we draw some conclusions based on the analysis presented.

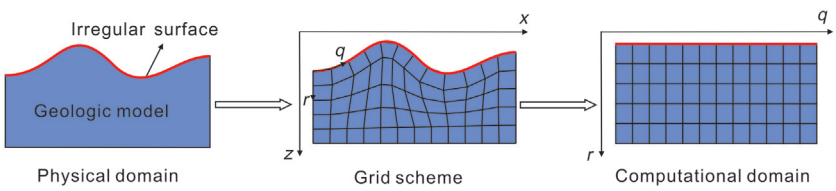

Figure 1. Schematic diagrams illustrating surface treatments. Surface-flattening scheme (Ma and Zhang, 2015): The geologic model is discretized using a boundary conforming grid and then undulated free surface is mathematically flattened by the transformation from Cartesian to curvilinear coordinates.

THEORY

Fast-sweeping method for TDEE

In a Cartesian coordinate system $\mathbf{x} = (x, z)$, the eikonal equation for isotropic media can be written as

$$\left(\frac{\partial T(\mathbf{x})}{\partial x}\right)^2 + \left(\frac{\partial T(\mathbf{x})}{\partial z}\right)^2 = \frac{1}{v^2(\mathbf{x})}, \tag{1}$$

where $T(x, z)$ is the first-arrival traveltime through an isotropic medium with velocity distribution $v(x, z)$.

To deal with irregular topography, we transform the Cartesian coordinate (x, z) to the curvilinear coordinate system (q, r) (Figure 1) (for more details, see Lan and Zhang, 2013b). The 2D TDEE in a curvilinear coordinate system can be formulated in a compact form as

$$a(\mathbf{q})\left(\frac{\partial T(\mathbf{q})}{\partial q}\right)^2 - 2c(\mathbf{q})\frac{\partial T(\mathbf{q})}{\partial q}\frac{\partial T(\mathbf{q})}{\partial r} + b(\mathbf{q})\left(\frac{\partial T(\mathbf{q})}{\partial r}\right)^2 = \frac{1}{v^2(\mathbf{q})}, \quad \mathbf{q}\in\Omega, \tag{2}$$

with the point-source condition:

$$T(\mathbf{q}_s) = 0. \tag{3}$$

The computational domain is denoted by $\Omega \subset \mathrm{R}^2$, and an arbitrary point in Ω is denoted by $\mathbf{q} = (q, r) \in R^2$. The parameters ($a$, b, and c) are topography-dependent. It is easy to demonstrate that $a, b > 0$ and $c^2 < ab$ (see the proof in Appendix A); therefore, TDEE is an elliptical anisotropic eikonal equation, which belongs to a class of convex Hamilton-Jacobian equations mathematically (Qian et al., 2007).

Recently, Zhou et al. (2020) introduce an efficient fast-sweeping method for solving the factored equation 2, which was originally developed

by Luo and Qian (2012). Here, we use it for forward modeling in the tomographic scheme. The following is a brief introduction to it.

The numerical solution of the TDEE is factorized into two multiplicative factors. We assume that T is the function of two multiplicative factors,

$$T = T_0\tau, \tag{4}$$

where T_0 is the known factor and τ is the evaluated factor. Then, we have

$$\nabla T = \nabla T_0\tau + T_0\nabla\tau. \tag{5}$$

Substituting it into TDEE, we have the FTDEE:

$$a\left(\frac{\partial T_0}{\partial q}\tau + T_0\frac{\partial \tau}{\partial q}\right)^2 - 2c\left(\frac{\partial T_0}{\partial q}\tau + T_0\frac{\partial \tau}{\partial q}\right) \cdot \left(\frac{\partial T_0}{\partial r}\tau + T_0\frac{\partial \tau}{\partial r}\right) + b\left(\frac{\partial T_0}{\partial r}\tau + T_0\frac{\partial \tau}{\partial r}\right)^2 = \frac{1}{v^2}. \tag{6}$$

The known factor T_0 is chosen analytically such that the unknown factor τ is smooth in the source neighborhood (Zhou et al., 2021). Therefore, τ can be accurately computed to recover the traveltime T, which eventually improves the accuracy of T compared to the solution obtained by solving equation 1 directly (Lan et al., 2018; Lan and Chen, 2018). A monotone fast-sweeping method has been developed to solve the resulting FTDEE discretized with the upwind finite-difference scheme, which treats the source singularity successfully and produces a clear first-order algorithm.

Adjoint-state method for TDEE

We first define the cost function as the least-squares norm of arrival time differences:

$$E(\boldsymbol{v}) = \frac{1}{2}\int_{\partial\Omega} |T(\boldsymbol{v},\boldsymbol{r}) - T^{\text{obs}}(\boldsymbol{r})|^2 d\boldsymbol{r}, \quad \boldsymbol{r}\in\partial\Omega, \tag{7}$$

where the integration is taken over receivers $\boldsymbol{r}$ located on the acquisition surface $\partial\Omega$. The terms $T(\boldsymbol{v},\boldsymbol{r})$ and $T^{\text{obs}}(\boldsymbol{r})$ denote the calculated traveltime for a particular medium with velocity distribution $\boldsymbol{v}(q,r)$ and the observed traveltime from measurements, respectively.

Mathematically, the minimization of equation 7 is a nonlinear problem, which is usually handled by local optimization methods. In this method, the descent direction at the nth iteration in the vicinity of the model $\boldsymbol{v}_n$ is given as

$$\boldsymbol{d}_n = -\boldsymbol{P}_n\nabla E(\boldsymbol{v}_n), \tag{8}$$

where $\boldsymbol{P}_n$ is a preconditioned matrix and $\nabla E(\boldsymbol{v}_n)$ is the gradient matrix of the cost function at $\boldsymbol{v}_n$.

The updated model $\boldsymbol{v}_{n+1}$ is determined by the initial model $\boldsymbol{v}_n$ and model perturbation $\Delta\boldsymbol{v}_n$ by the following expression:

$$\boldsymbol{v}_{n+1} = \boldsymbol{v}_n + \Delta\boldsymbol{v}_n = \boldsymbol{v}_n + \alpha_n\boldsymbol{d}_n, \tag{9}$$

where α_n is the step length to update the model in the search direction, which can be estimated by the exact parabolic search method (Liu et al., 2017).

Here, we calculate the gradient of the misfit function, equation 7, in the framework of Lagrangian formalism (Leung and Qian, 2006; Plessix, 2006). First, we define the perturbation of the velocity as $\partial\boldsymbol{v}$, which causes a corresponding change in the arrival time ∂T. Therefore, the change of the misfit function can be expressed as

$$\partial E = \int_{\partial\Omega}(T - T^{\text{obs}})\partial T d\boldsymbol{r}. \tag{10}$$

The perturbation in velocity is related to the perturbation of arrival time obtained by differentiating equation 2:

$$(aT_q - cT_r)\partial T_q + (bT_r - cT_q)\partial T_r = -\frac{1}{v^3}\partial v, \tag{11}$$

where $T_q = \partial T/\partial q$ and $T_r = \partial T/\partial r$.

We rewrite the change of the misfit function through the Lagrange formulation as

$$\partial L = \int_{\partial\Omega}(T - T^{\text{obs}})\partial T d\mathbf{q} + \int_{\Omega}\lambda((aT_q - cT_r)\partial T_q + (bT_r - cT_q)\partial T_r + \frac{1}{v^3}\partial v)d\mathbf{q}. \tag{12}$$

Integrating the second part of the right side with divergence theorem leads to

$$\partial L = \int_{\partial\Omega}(T - T^{\text{obs}})\partial T d\mathbf{q} + \int_{\partial\Omega}(\mathbf{n}\cdot\mathbf{L})\lambda\partial T d\mathbf{q} + \int_{\Omega}\nabla\cdot(-\lambda\mathbf{L})\partial T d\mathbf{q} + \int_{\Omega}\frac{\lambda}{v^3}\partial v d\mathbf{q}, \tag{13}$$

where

$$\mathbf{L}(\mathbf{q}) = [aT_q - cT_r, bT_r - cT_q]. \tag{14}$$

The term $\mathbf{L}(\mathbf{q})$ represents the group velocity vector along the raypath initiated from the source to the receiver (Qian et al., 2007; Luo and Qian, 2012). For anisotropic TDEE, the group velocity vector has a different direction from that of the phase velocity vector. For an isotropic medium with a flat free surface, $\mathbf{L}(\mathbf{q})$ can be reduced to the traveltime gradient (T_q, T_r), as described by Leung and Qian (2006).

We choose a multiplier λ that satisfies the following equation and boundary condition:

$$\nabla\cdot(-\lambda(\mathbf{q})\mathbf{L}(\mathbf{q})) = 0, \quad \mathbf{q}\in\Omega, \tag{15a}$$

$$\mathbf{n}\cdot\mathbf{L}(\mathbf{q})\lambda(\mathbf{q}) = T^{\text{obs}} - T, \quad \mathbf{q}\in\partial\Omega, \tag{15b}$$

where $\mathbf{n}$ is the normal vector perpendicular to the acquisition surface $\partial\Omega$ in the computational domain. The gradient of the objective function can be calculated by

$$\frac{\partial E}{\partial v} = \frac{\partial L}{\partial v} = \int_{\Omega} \frac{\lambda}{v^3} d\mathbf{q}. \tag{16}$$

The multiplier λ and equation 15a are also called the adjoint solution and the topography-dependent adjoint-state equation, respectively. In fact, equation 15a also can be obtained by a direct transformation of the adjoint-state equation from Cartesian to curvilinear coordinates (see Appendix B). Like the eikonal solver, the adjoint-state algorithm is a combination of a local finite-difference operator to estimate λ and fast-sweeping method to propagate the residuals $T^{\text{obs}} - T$ back into the model (see Appendix C). By replacing traveltime residuals with a fixed value c in equation 15b, we could obtain a preconditioner $\boldsymbol{P}_n$ in equation 8 to speed up the convergence of the algorithm, which will also reduce the computational cost and improve the resolution (Benaichouche et al., 2015; Li et al., 2017).

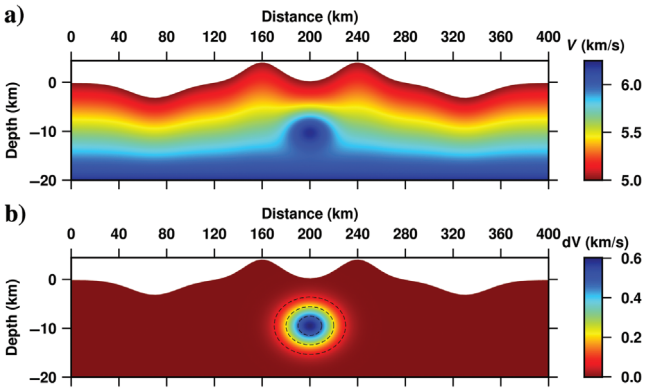

Figure 2. Velocity model with wavy topography used to illustrate the computation of the gradient of the misfit function. (a) Exact velocity model and (b) perturbation to be retrieved. The dashed contours mark the location and shape of the positive Gaussian anomaly.

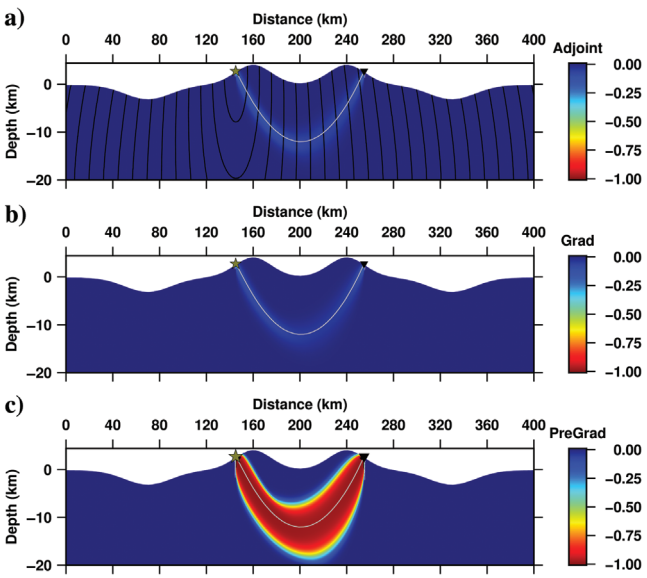

Figure 3. (a) Adjoint-state solution, (b) gradient, and (c) preconditioned gradient for a single source-receiver pair obtained by the adjoint-state method. The posterior raypaths are shown with a gray line for the source-receiver pair. The dark yellow star marks the seismic source, whereas the black inverted triangle indicates the receiver on the surface. For plotting, each image is normalized to have a maximum value of one.

NUMERICAL EXPERIMENTS

Gradient calculation with the adjoint-state method

We illustrate the key process of calculating the gradient of the misfit function through a simple model with complex topography. The irregular topography consists of two central hills separated by a central valley and lateral valleys on both sides of the hills. The horizontal extent of the model is 400 km. The wavy topography of the model fluctuates between −3 and 4.2 km and the model depth is 20 km. We use the 800 × 40 boundary conforming cells with grid spacing approximately 0.5 × 0.5 km to discretize the model. Up to 20 shots are fired virtually at equally spaced points on the surface, which are recorded by 200 receivers evenly deployed on the irregular surface. For this acquisition, we consider the rays with large source-receiver offset hitting the bottom of the velocity model. The background seismic velocity gradually increases from 5.0 to 6.2 km/s with depth. A Gaussian anomaly with a maximum perturbation of 0.6 km/s is embedded in the middle of the model (Figure 2).

The background model is regarded as the initial model to start the inversion. First, we just consider a single source-receiver pair, placed on the surface at 145 and 255 km, respectively. First-arrival traveltimes are obtained by solving equation 2 on the true and initial models to get the observed traveltimes and residuals. After obtaining the traveltime residuals, we could initialize the adjoint-state solution at receivers by using equation 15b. Then, the fast-sweeping method is used to calculate the adjoint-state solution for the whole model by solving equation 15a. The adjoint-state solution of the first iteration with first-arrival traveltimes and raypaths superimposed is shown in Figure 3a. We see that the adjoint-state solution can be interpreted as the back-propagation of traveltime residuals along the raypath from the receiver to the source positions (Taillandier et al., 2009). Then, the gradient of the misfit function for a single source is obtained by scaling the adjoint-state field according to equation 16 (Figure 3b). Next, a preconditioned gradient with source and receiver effects minimized is shown in Figure 3c.

For all sources and receivers, the total gradient is the sum of all source contributions. Even though the gradient is calculated by the adjoint-state method, it also requires smoothing to prevent the inversion from getting trapped into local minima and to suppress the strong source signature in the computed gradient (Taillandier et al., 2009; Waheed et al., 2016). If the gradient is not smoothed, this may lead the algorithm to nonphysical updates. The smoothing is usually performed as a filter in many classic tomography algorithms that are based on ray-tracing methods. The gradient and the preconditioned gradient before and after using a Gaussian smoother with a filter length of 10 grid points (approximately 5 km) are shown in Figure 4, and the horizontal and vertical profiles through the center of the anomaly are shown in Figure 5. The source signature can be easily observed in the computed gradient, as shown in Figure 4a. After smoothing the gradient, the undesirable signature around the source is significantly eliminated as shown in Figure 4c, although the

maximum gradient is shallower than its true location. However, from Figure 4b and 4d, we see that the gradient of multiple source-receiver couples is significantly improved by preconditioning, and the maximum of the preconditioned gradient is nearly in the center of the anomaly. We also observe that the preconditioner scales and sharpens the image of the gradient effectively into an actual model update (Figure 5).

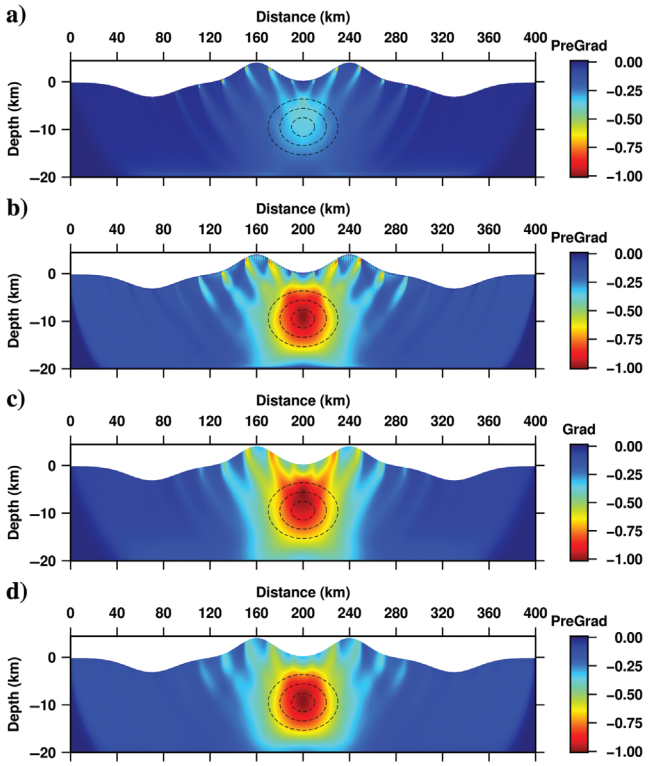

Figure 4. (a and c) Gradient and preconditioned gradients for all source-receiver couples, whereas (b and d) correspond to the gradient and preconditioned gradients after using Gaussian smoothing with a filter length of 10 grid points along both dimensions. The dashed contours mark the location and shape of the positive Gaussian anomaly. For plotting, each value is normalized to have a maximum value of one.

Anomaly synthetic model

We validate our method with a series of models with complex topography, including hill, valley, slow wavy, and sharp wavy topography, as shown in Figure 6. For every numerical model, a Gaussian-shaped positive perturbation with a maximum velocity of 0.6 km/s and a negative anomaly with a minimum velocity of −0.6 km/s is embedded in a gradient-velocity model varying from

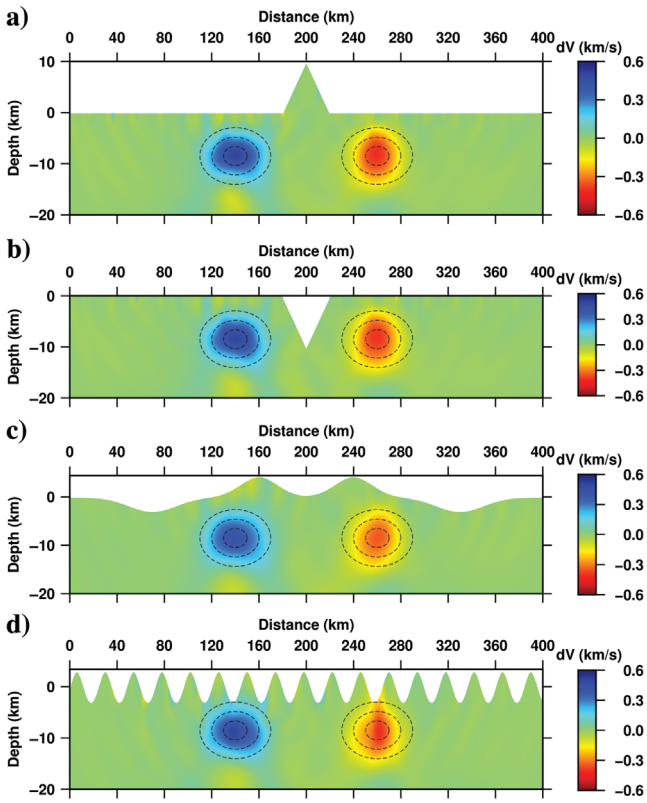

Figure 6. Synthetic models with two Gaussian anomalies and complex topography: (a) hill, (b) valley, (c) slow wavy, and (d) sharp wavy. The dashed contours mark the location and shape of the Gaussian anomalies.

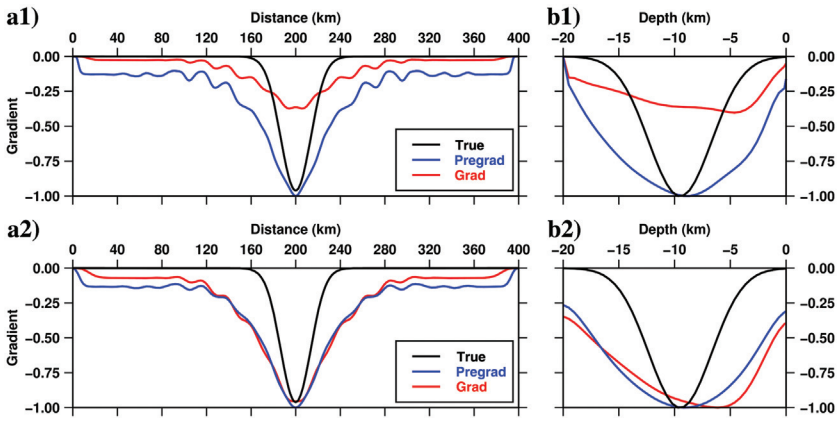

Figure 5. (a) The horizontal and (b) vertical profiles of normalized gradient (the red line), preconditioned gradient (the blue line), and negative perturbation (the black line) through the center of the Gaussian anomaly. The first and second rows denote the results without and with Gaussian smoothing.

5.0 to 6.2 km/s with depth. For inversion, the background model is considered as the starting model. In view of the quality of results and the cost of computation, we start the inversion by applying a strong Gaussian smoother with a filter length of 20 grid points (approximately 10 km) along both dimensions on the gradient for each iteration, and we gradually decrease the filter length (filter length: 5, 2.5, 1.25, and 0 km) after five iterations until traveltime residuals converge. The inverted models are shown in Figure 6, whereas the profiles across the centers of anomalies are presented in Figure 7. We could see that the shape and strength of Gaussian anomalies are essentially retrieved without the impact of complex topography, whereas smearing effects are obvious due to insufficient ray coverage from several directions. Figure 8 shows the normalized traveltime residuals versus the number of iterations: The traveltime residuals gradually stabilize and converge after eight iterations for all tests, which indicates the rapid convergence of the proposed algorithm even under a dramatically undulating surface.

Complex synthetic model

The new method is also tested on a realistic-sized acquisition setup using a complex synthetic model modified from Liu et al. (2009). The entire profile has a length of 400 km and a depth of 15 km, which is characterized by large variations in velocity pattern and topography (Figure 9a). We discretize the model into 800 × 30 boundary-conforming cells with grid spacing approximately 0.5 × 0.5 km. In this case, 20 shots and 200 receivers are evenly deployed on the surface with an interval of 20 and 2 km, respectively. The initial model with a constant vertical velocity gradient is displayed in Figure 9b. The inversion result is shown in Figure 9c. The comparison of Figure 9a–9c shows that long-wavelength features of the whole model have been well recovered by inversion, except on the edges where ray coverage is poor and becomes worse with increasing depth. Figure 10 compares several velocity profiles from the initial, inverted, and true velocity models at different locations along the vertical dimension of: 150, 200, and 300 km and horizontal dimension of: −0.5 and −1.5 km. The agreement between the true model and the inverted model is significantly better compared to the initial model. This synthetic model indicates that our tomographic method is quite flexible in accommodating velocity variations and contrasting topographies.

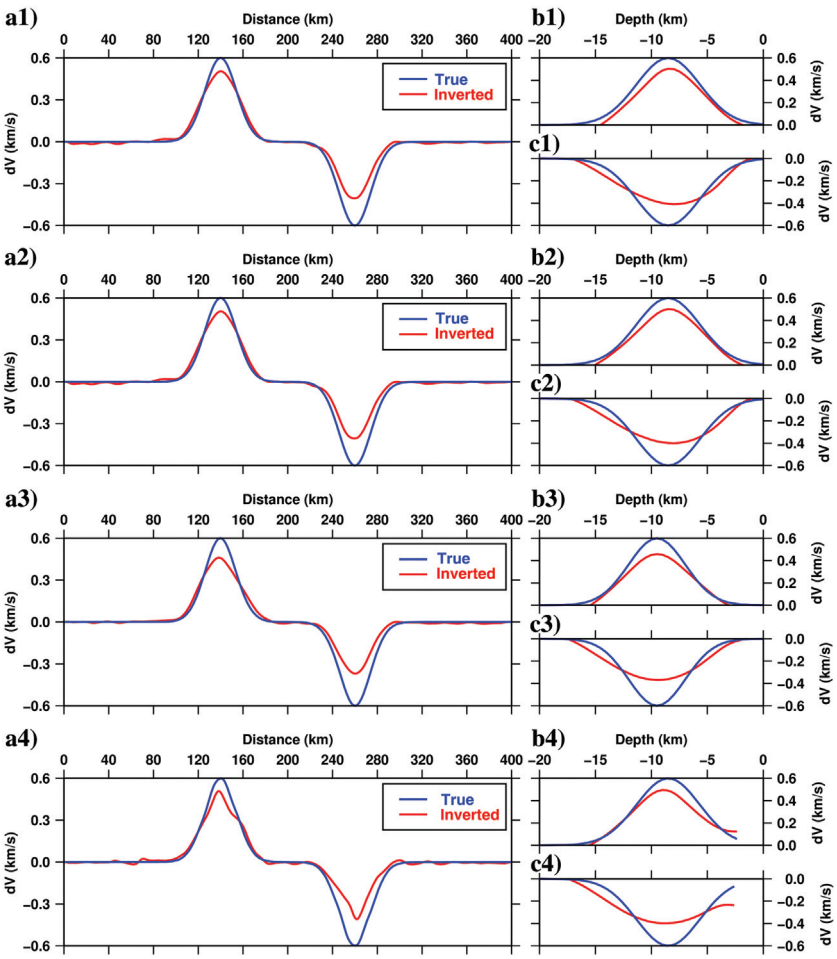

Figure 7. (a) The horizontal and (b and c) vertical profiles of true (the blue line) and inverted (the red line) perturbations for models with (a1-c1) hill, (a2-c2) valley, (a3-c3) wave, and (a4-c4) sin topography.

Application to real data

With the purpose of applying our working scheme to real data, we make use of a 430 km wide-angle seismic profile between Jingtai and Hezuo, which was deployed in the direction N45°E from the eastern Tibetan Plateau to the Qilian orogenic block in western China (Figure 11; Zhang et al., 2013; Ma and Zhang, 2015). In total, 11 shots are fired at different sites along the profile with an average horizontal spacing of 50 km. A set of 200 portable 3C digital seismographic stations with a spacing of 2 km is used to record the data. Pg-wave arrival (first arrival) traveltimes are picked (with an estimated error of approximately 0.05 s) from 11 common-shot gathers.

In the considered area, topography varies sharply and gradually decreases from just more than 3.5 km to almost 1.5 km (Figure 10). We discretize the upper-crust model using 860 × 460 boundary conforming cells adjusted to the real topography, with a spacing size of approximately 0.5 km horizontally and vertically. To start the computations, we use an initial model with a linearly increasing velocity from 5.0 to 6.2 km/s. For comparison, in Figure 12 we show the traveltime residuals from the initial and the inverted models, in which the improvement in the traveltime fit validates the accuracy and stability of the proposed method.

To confirm the main features of the result, we conduct a checkerboard test to evaluate resolution based on the identical surface topography and the same distribution of sources and locations with real acquisition geometry. We artificially add perturbations with a spatial scale of 25 × 13.33 km to the background model with linearly increasing velocity from 5.0 to 6.2 km/s, using the formula 0.3 × sin (x) × sin (z). The synthetic traveltimes

are calculated from the checkerboard model, and the background models with positive speed gradients are used as initial models to start the inverse computation. As shown in Figures 13 and 14, the comparison between the synthetic and inverted perturbations indicates that the shallow velocity characteristics of checkerboard perturbation within 10 km can be well recovered, whereas the partial deeper structure is only partially illuminated beneath 130–190 km and 250–320 km.

Then, the inverted velocity model is shown in Figure 15. This compressional wave (P-wave) velocity model has obvious vertical stratification and horizontal blocking characteristics. In the vertical direction, it is clearly divided into two layers, namely the sedimentary layer and the crystalline basement. According to Zhang et al. (2013), we consider the boundary of the two layers to be at the isoline of 5.8 km/s. From south to north, this model reveals the geometry of a sedimentary basin and fault, and matches the tectonic division of the Qaidam-Kunlun-West Qinling belt, the central and northern Qilian, and the Alax block along the profile. In the following, we discuss the shallow velocity model beneath several tectonic units.

1) The segment going from the south end up to approximately 120 km northward belongs to the Qaidam-Eastern Kunlun-West Qinling terrain. The sedimentary layer can be divided into the southern part with a P-wave velocity less than 5.3 km/s and northern parts with a P-wave velocity of approximately 5.5 km/s. This is consistent with the widespread deposition of Middle-Upper Carboniferous shallow-marine carbonate rocks in southern and bedrock exposures scattered along its northernmost edge (Zhang et al., 2013).
2) The segment between 120 and 330 km belongs to the central Qilian orogenic belt. There are obvious differences in the structure of the south and north Maxianshan fault, which also can be observed in receiver function (Ye et al., 2015) and Bouguer gravity anomaly (Guo et al., 2016). Beneath the south, the sedimentary layer shows an average velocity of approximately 5.0 km/s, which corresponds to the Linxia Basin. Beneath the north, the sediment has a P-wave velocity of less than 4.4 km/s and becomes approximately 5.5 km/s further north.
3) The segment between 330 and 380 km belongs to the northern Qilian block. We observe that there are 3–4 km thick sediments, which cover the crystalline basement with a P-wave velocity of 5.8–6.0 km/s (Zhang et al., 2013).
4) The segment from approximately 380 km to the north end belongs to the Alashan depression. At the end of the profile, we observe that the depression has a thicker sediment layer with a P-wave velocity less than 5.8 km/s, compared to the sediment beneath North Qilian block.

In Figure 15a, we display the results obtained by Ma and Zhang (2015) using a conventional method (Hole et al., 2001), in which the topography is handled by the model expansion method. From the comparison between the two results, we see that the main velocity characteristics are similar, whereas the proposed method is better than the conventional method in the following respects: (1) The detachment beneath Linxia Basin is more finely delineated in our

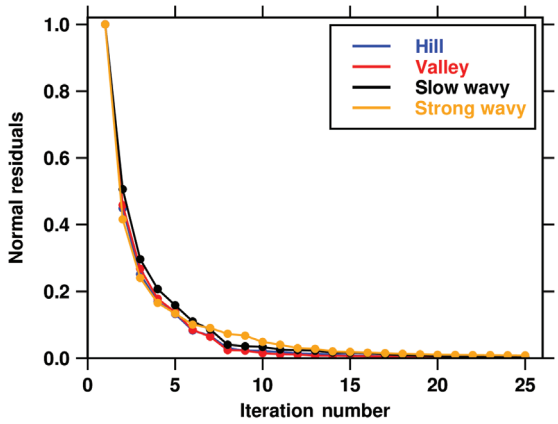

Figure 8. Normalized traveltime residual versus the number of iterations after inverting the model with the two Gaussian anomalies under the hill, valley, slow wavy, and sharp wavy topography.

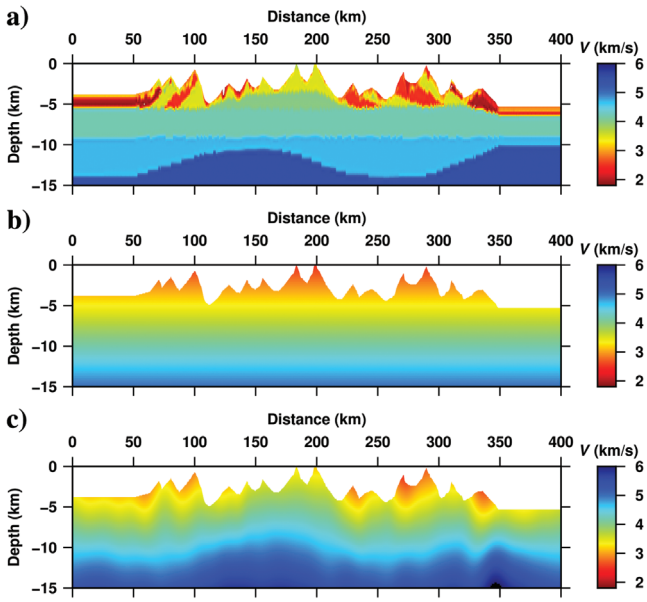

Figure 9. (a) A synthetic model with complex topography, (b) initial model, and (c) inverted model.

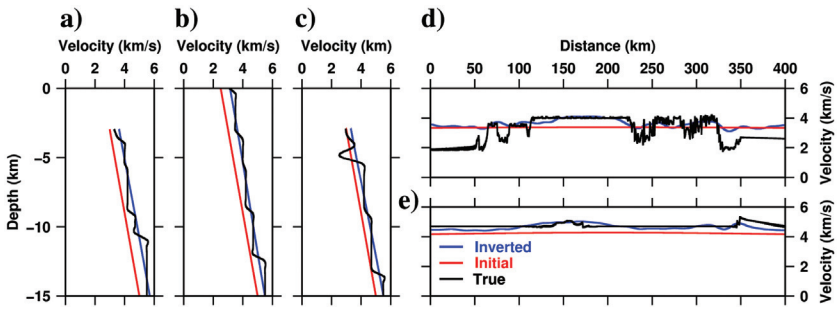

Figure 10. Velocity logs for the initial (red), inverted (blue), and true (black) velocity models at different vertical locations of: (a) 150 km, (b) 200 km, and (c) 300 km, and horizontal locations of: (d) −0.5 km and (e) −1.0 km, respectively.

method than in conventional imaging; (2) the uplifted crystalline basement within the Maxianshan fault is accurate in our imaging, whereas the crystalline basement (isoline 5.8 km/s) in the previous study is confusing; (3) the finer bedrock exposure in the northern margin fault is delineated by isoline 5.8 km/s in our study, whereas it is problematic in conventional imaging; and (4) the velocity characteristics corresponding to the northern fault and Tianjingshan fault are more visible in this study (Guo et al., 2016) (Figure 15c). All of the details in the velocity pattern indicate that the P-wave velocity model produced by our method should be more precise in resolving the main features along this wide-angle profile. It should be noted that currently we only use the first-arrival traveltimes. A more accurate high-resolution structure and comprehen-

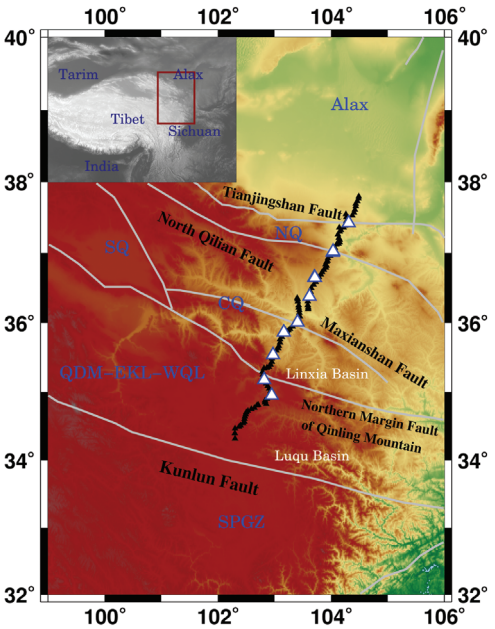

Figure 11. Tectonic map of a wide-angle seismic profile in the approximate direction N45°E going south–north from the northeastern Tibetan Plateau to the Qilian block in western China. The inset, on the top left corner, contains a rectangle drawn on a map that allows locating the region crossed by the profile (eastern margin of Tibet) (Zhang et al., 2013). The white triangles mark shot points and small black triangles indicate receiver positions. The gray line shows faults crossed by the seismic profile. Main tectonic units from north to south: Alax, Alax depression; NQ, northern Qilian block; SQ, south Qilian block; CQ, central Qilian block; QDM-EKL-WQL, Qaidam-East Kunlun-West Qinling block; and SPGZ, Songpan-Ganzi block.

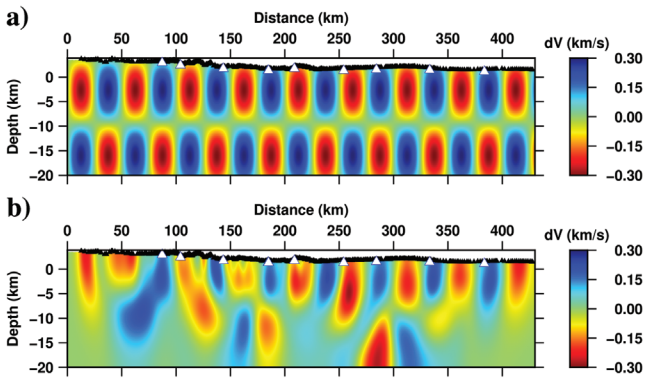

Figure 13. Checkerboard resolution test. (a) Input checkerboard model. (b) Inverted checkerboard model. The spatial scale of perturbation is 25 × 13.33 km. The black and white triangles denote receiver and shot positions, respectively.

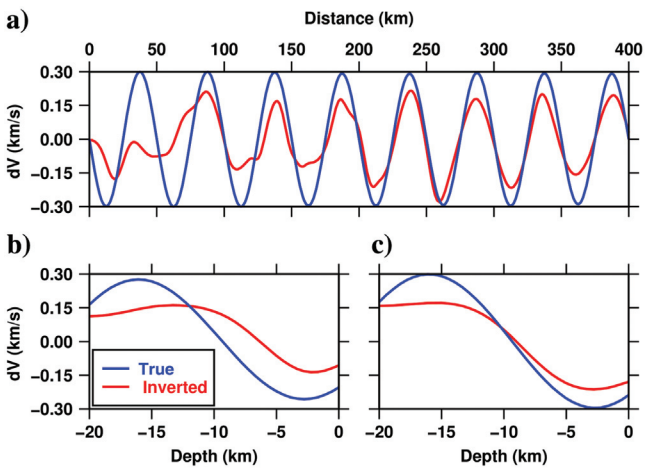

Figure 14. Horizontal profile (a) through the center of the first row of true and inverted checkerboard perturbations, whereas vertical profiles are located at (b) y = 159 km and (c) y = 312 km, respectively.

Figure 12. Distribution of first-arrival traveltime residuals. The red and blue crosses denote the initial and final inverted traveltime residuals, respectively. The top plate shows the elevation along the profile with the tectonic units labeled. The black and white triangles denote receiver and shot positions, respectively.

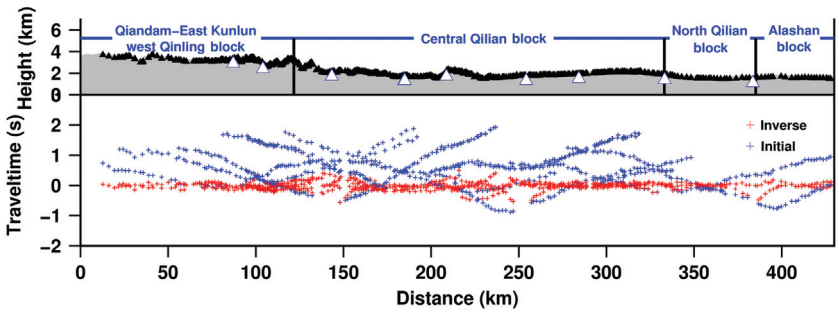

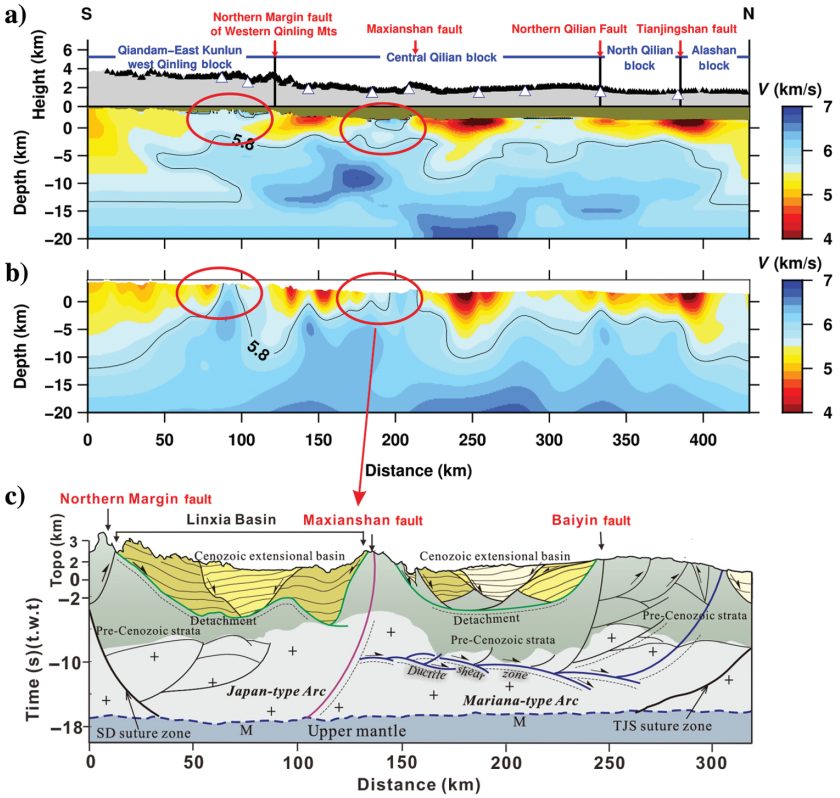

Figure 15. Upper crustal velocity model obtained from topography-dependent eikonal tomography. (a) The velocity model obtained by the conventional Hole's method (Ma and Zhang, 2015). (b) The velocity model obtained by topography-dependent eikonal tomography. (c) The crustal-scale structural features of the Maxianshan fault zone from the deep seismic reflection profile (Guo et al., 2016), which coincides with the wide-angle seismic profile in our study.

sive geodynamic implications require joint use of the first-arrival and reflected traveltimes.

CONCLUSION

In this paper, we have developed a new matrix-free eikonal tomography scheme that allows modeling seismic velocity structures with irregular topography. To obtain first-arrival traveltimes, we numerically solve the TDEE once formulated in curvilinear coordinates using a factored fast-sweeping solver. The adjoint-state method is introduced to obtain the gradient of nonlinear misfit function, which avoids using the cumbersome ray-tracing technique in curvilinear coordinates. At present, we implement the preconditioned steepest-descent method for the velocity model inversion, and we could improve the optimizer using the preconditioned nonlinear limited-memory Broyden-Fletcher-Goldfarb-Shanno (L-BFGS) method or preconditioned truncated Newton method in the next study.

The new tomography scheme has been evaluated through a series of synthetic models and field data. The results support the effectiveness and reliability of the proposed approach in different situations. At this stage, our study is limited to first-arrival traveltimes, but its extension to reflected wave and critical refractions is quite meaningful in the exploration of subsurface environments where prominent boundaries often prevail.

ACKNOWLEDGMENTS

The authors would like to thank L. Chen, J. Huang, S. Luo, and B. Tavakoli F. for their constructive comments and enthusiastic help. Fruitful discussions with Y. Liu at Tongji University are also greatly appreciated. In addition, we thank T. Ma for providing the Jingtai-Hezuo wide-angle data and X. Guo for sharing Figure 15c. This research is supported by the National Natural Science Foundation of China (grant nos. 42022028, 41674095, and 4184065), the Open Fund Project State Key Laboratory of Lithospheric Evolution (SKL-YT201802), and the Strategic Priority Research Program (XDA20070302).

DATA AND MATERIALS AVAILABILITY

Data associated with this research are available and can be obtained by contacting the corresponding author.

APPENDIX A

THE PROOF OF SYMMETRIC POSITIVE DEFINITE OF COORDINATE FOR TDEE

We present a proof that coordinate transformation for TDEE can always be written as a symmetric positive definite matrix. The TDEE is shown as follows:

$$a(\mathbf{q})\left(\frac{\partial T(\mathbf{q})}{\partial q}\right)^2-2c(\mathbf{q})\frac{\partial T(\mathbf{q})}{\partial q}\frac{\partial T(\mathbf{q})}{\partial r}+b(\mathbf{q})\left(\frac{\partial T(\mathbf{q})}{\partial r}\right)^2=\frac{1}{v^2(\mathbf{q})}, \tag{A-1}$$

where coefficients $a(\mathbf{q})$, $b(\mathbf{q})$, and $c(\mathbf{q})$ are topography-dependent parameters, and they are functions of metric derivatives:

$$a(\mathbf{q})=\frac{x_r^2+z_r^2}{J^2},\quad b(\mathbf{q})=\frac{x_q^2+z_q^2}{J^2},\quad c(\mathbf{q})=\frac{x_q x_r+z_q z_r}{J^2}, \tag{A-2}$$

where x_q denotes the partial derivative $x_q=\partial x(q,r)/\partial q$, and similar nomenclature for other metric derivatives (x_r, z_q, z_r). The term $J=x_q z_r-x_r z_q$ in equation A-2 is the Jacobian of the transformation from Cartesian to curvilinear coordinates.

From the preceding definitions, we could conclude that $a(\mathbf{q})$ and $b(\mathbf{q})$ are always greater than zero. In addition, we could get the following inequality:

$$a(\mathbf{q})b(\mathbf{q}) - c(\mathbf{q})^2 = \frac{(x_r^2 + z_r^2)}{J^2}\frac{(x_q^2 + z_q^2)}{J^2} - \left(\frac{x_q x_r + z_q z_r}{J^2}\right)^2 = \frac{(x_r z_q - x_q z_r)^2}{J^4} > 0. \tag{A-3}$$

The transformation in equation A-1 also could be written as a matrix formation:

$$\nabla T(\mathbf{q}) M(\mathbf{q}) \nabla T(\mathbf{q})^t = \frac{1}{v^2(\mathbf{q})}, \tag{A-4}$$

where t is transport and $M(\mathbf{q}) = \begin{pmatrix} a(\mathbf{q}) - c(\mathbf{q}) \\ -c(\mathbf{q}) b(\mathbf{q}) \end{pmatrix}$ is a symmetric matrix modeling the anisotropy. The characteristic equation of matrix $M(\mathbf{q})$ is

$$(a(\mathbf{q}) - \lambda)(b(\mathbf{q}) - \lambda) - c(\mathbf{q})^2 = 0. \tag{A-5}$$

The discriminant term is

$$\Delta = (a(\mathbf{q}) + b(\mathbf{q}))^2 - 4(a(\mathbf{q})b(\mathbf{q}) - c(\mathbf{q})^2) = (a(\mathbf{q}) - b(\mathbf{q}))^2 + c(\mathbf{q})^2 > 0, \tag{A-6}$$

so we could find two different roots of this quadratic equation as λ_1 and λ_2, which means two eigenvalues of matrix $M(\mathbf{q})$:

$$\lambda_1 = \frac{(a(\mathbf{q}) + b(\mathbf{q})) + \sqrt{(a(\mathbf{q}) - b(\mathbf{q}))^2 + 4c(\mathbf{q})^2}}{2} > 0, \tag{A-7}$$

$$\begin{aligned} \lambda_2 &= \frac{(a(\mathbf{q}) + b(\mathbf{q})) - \sqrt{(a(\mathbf{q}) - b(\mathbf{q}))^2 + 4c(\mathbf{q})^2}}{2} \\ &= \frac{\sqrt{(a(\mathbf{q}) + b(\mathbf{q}))^2 + 4c(\mathbf{q})^2 - 4c(\mathbf{q})^2} - \sqrt{(a(\mathbf{q}) - b(\mathbf{q}))^2 + 4c(\mathbf{q})^2}}{2} \\ &> \frac{\sqrt{(a(\mathbf{q}) + b(\mathbf{q}))^2 - 4a(\mathbf{q})b(\mathbf{q}) + 4c(\mathbf{q})^2} - \sqrt{(a(\mathbf{q}) - b(\mathbf{q}))^2 + 4c(\mathbf{q})^2}}{2} \\ &= 0. \end{aligned} \tag{A-8}$$

Because the λ_1 and λ_2 are positive, $M(\mathbf{q})$ is always a symmetric positive matrix and there are no assumptions on the curvilinear coordinate transformation in practice.

APPENDIX B

DERIVATION OF THE TOPOGRAPHY-DEPENDENT ADJOINT-STATE EQUATION FROM THE CLASSIC ADJOINT-STATE EQUATION

In the Cartesian coordinate system (x, z) and for isotropic media, the adjoint-state equation takes the following form (Leung and Qian, 2006; Huang and Bellefleur, 2012):

$$\frac{\partial}{\partial x}\left(-\frac{\partial T}{\partial x}\lambda\right) + \frac{\partial}{\partial z}\left(-\frac{\partial T}{\partial z}\lambda\right) = 0, \tag{B-1}$$

where $\lambda(x, z)$ is the adjoint-state solution that can be read as back-propagation of traveltime residuals along the raypaths to the source position.

Using the coordinate transformation (Lan and Zhang, 2013b), we also derive the adjoint-state equation in curvilinear coordinate systems (q, r) as

$$\frac{\partial\left(\left(-\frac{z_r^2 + x_r^2}{J^2}\frac{\partial T}{\partial q} + \frac{z_r z_q + x_q x_r}{J^2}\frac{\partial T}{\partial r}\right)\cdot\lambda\right)}{\partial q} + \frac{\partial\left(\left(-\frac{z_q^2 + x_q^2}{J^2}\frac{\partial T}{\partial r} + \frac{z_r z_q + x_q x_r}{J^2}\frac{\partial T}{\partial q}\right)\cdot\lambda\right)}{\partial r} = 0. \tag{B-2}$$

By substituting topography-dependent coefficients (a, b, c) into equation B-2, we obtain

$$\frac{\partial\left(\left(-a\frac{\partial T}{\partial q} + c\frac{\partial T}{\partial r}\right)\cdot\lambda\right)}{\partial q} + \frac{\partial\left(\left(-b\frac{\partial T}{\partial r} + c\frac{\partial T}{\partial q}\right)\cdot\lambda\right)}{\partial r} = 0, \tag{B-3}$$

which can be rewritten more concisely as

$$\frac{\partial}{\partial q}(\alpha\lambda) + \frac{\partial}{\partial r}(\beta\lambda) = 0, \tag{B-4}$$

where

$$\alpha = -a\frac{\partial T}{\partial q} + c\frac{\partial T}{\partial r}, \tag{B-5a}$$

$$\beta = -b\frac{\partial T}{\partial r} + c\frac{\partial T}{\partial q}. \tag{B-5b}$$

The α and β are the group velocity in the horizontal and vertical directions in the computational domain, respectively. Equation B-4 is the same as equation 15a, which is a so-called topography-dependent adjoint-state equation. When the surface is flat, equation B-4 can be reduced to the classic adjoint-state equation B-1.

APPENDIX C

CALCULATION OF TOPOGRAPHY-DEPENDENT ADJOINT-STATE EQUATION

For a computational cell centered at (q_i, r_j), discretizing equation B-4 using a first-order finite-difference approximation in the conservative form yields

$$\frac{\alpha_{i+\frac{1}{2},j}\lambda_{i+\frac{1}{2},j} - \alpha_{i-\frac{1}{2},j}\lambda_{i-\frac{1}{2},j}}{\Delta q} + \frac{\beta_{i,j+\frac{1}{2}}\lambda_{i,j+\frac{1}{2}} - \beta_{i,j-\frac{1}{2}}\lambda_{i,j-\frac{1}{2}}}{\Delta r} = 0, \tag{C-1}$$

where Δq and Δr define the computational grid spacing in the q and r directions, respectively. The values of α and β are specified at intermediate positions, leading to

$$\alpha_{i\pm\frac{1}{2},j} = -a_{i\pm\frac{1}{2},j}\left(\frac{\partial T}{\partial q}\right)_{i\pm\frac{1}{2},j} + c_{i\pm\frac{1}{2},j}\left(\frac{\partial T}{\partial r}\right)_{i\pm\frac{1}{2},j}, \tag{C-2a}$$

$$\beta_{i,j\pm\frac{1}{2}} = -b_{i,j\pm\frac{1}{2}}\left(\frac{\partial T}{\partial r}\right)_{i,j\pm\frac{1}{2}} + c_{i,j\pm\frac{1}{2}}\left(\frac{\partial T}{\partial q}\right)_{i,j\pm\frac{1}{2}}. \tag{C-2b}$$

Comparing with the isotropic adjoint tomography, in which the group velocity is the same as the phase velocity, we face more complexity in the calculation of α and β on the interface. The spatial gradient maps need to be calculated on the horizontal q and vertical interfaces r, respectively. These stencils lead us toward the approximations of α on the horizontal interfaces as (Tavakoli, 2017)

$$\alpha_{i-\frac{1}{2},j} = -\frac{a_{i-1,j}+a_{i,j}}{2}\frac{T_{i,j}-T_{i-1,j}}{\Delta q} + \frac{c_{i-1,j}+c_{i,j}}{2}\frac{T_{i-1,j+1}+T_{i,j+1}-T_{i-1,j-1}-T_{i,j-1}}{4\Delta r}, \tag{C-3a}$$

$$\alpha_{i+\frac{1}{2},j} = -\frac{a_{i+1,j}+a_{i,j}}{2}\frac{T_{i+1,j}-T_{i,j}}{\Delta q} + \frac{c_{i+1,j}+c_{i,j}}{2}\frac{T_{i+1,j+1}+T_{i,j+1}-T_{i+1,j-1}-T_{i,j-1}}{4\Delta r}, \tag{C-3b}$$

and β on the vertical interfaces as

$$\beta_{i,j-\frac{1}{2}} = -\frac{b_{i,j-1}+b_{i,j}}{2}\frac{T_{i,j}-T_{i,j-1}}{\Delta r} + \frac{c_{i,j-1}+c_{i,j}}{2}\frac{T_{i+1,j-1}+T_{i+1,j}-T_{i-1,j-1}-T_{i-1,j}}{4\Delta q}, \tag{C-4a}$$

$$\beta_{i,j+\frac{1}{2}} = -\frac{b_{i,j+1}+b_{i,j}}{2}\frac{T_{i,j+1}-T_{i,j}}{\Delta r} + \frac{c_{i,j+1}+c_{i,j}}{2}\frac{T_{i+1,j+1}+T_{i+1,j}-T_{i-1,j+1}-T_{i-1,j}}{4\Delta q}. \tag{C-4b}$$

Let us introduce the following notation:

$$\alpha^{\pm}_{i+\frac{1}{2},j} = \frac{\alpha_{i+\frac{1}{2},j} \pm |\alpha_{i+\frac{1}{2},j}|}{2}, \qquad \alpha^{\pm}_{i-\frac{1}{2},j} = \frac{\alpha_{i-\frac{1}{2},j} \pm |\alpha_{i-\frac{1}{2},j}|}{2}, \tag{C-5a}$$

$$\beta^{\pm}_{i,j+\frac{1}{2}} = \frac{\beta_{i,j+\frac{1}{2}} \pm |\beta_{i,j+\frac{1}{2}}|}{2}, \qquad \beta^{\pm}_{i,j-\frac{1}{2}} = \frac{\beta_{i,j-\frac{1}{2}} \pm |\beta_{i,j-\frac{1}{2}}|}{2}. \tag{C-5b}$$

Then, the values of λ on the interface, $\lambda_{i\pm1/2,j}$ and $\lambda_{i,j\pm1/2}$, are determined according to the propagation of characteristics. In the case $\alpha_{i+1/2,j} > 0$, the characteristic for determining λ goes from the left side of the interface to the right side, and this means that the value $\lambda_{i,j}$ can be used to define $\lambda_{i+1/2,j}$. Otherwise, we use $\lambda_{i+1,j}$ to determine $\lambda_{i+1/2,j}$.

Next, equation B-1 becomes

$$\frac{(\alpha^{+}_{i+\frac{1}{2},j}\lambda_{i,j} + \alpha^{-}_{i+\frac{1}{2},j}\lambda_{i+1,j}) - (\alpha^{+}_{i-\frac{1}{2},j}\lambda_{i-1,j} + \alpha^{-}_{i-\frac{1}{2},j}\lambda_{i,j})}{\Delta q} + \frac{(\beta^{+}_{i,j+\frac{1}{2}}\lambda_{i,j} + \beta^{-}_{i,j+\frac{1}{2}}\lambda_{i,j+1}) - (\beta^{+}_{i,j-\frac{1}{2}}\lambda_{i,j-1} + \beta^{-}_{i,j-\frac{1}{2}}\lambda_{i,j})}{\Delta r} = 0, \tag{C-6}$$

or equivalently,

$$\left(\frac{\alpha^{+}_{i+\frac{1}{2},j} - \alpha^{-}_{i-\frac{1}{2},j}}{\Delta q} + \frac{\beta^{+}_{i,j+\frac{1}{2}} - \beta^{-}_{i,j-\frac{1}{2}}}{\Delta r}\right)\lambda_{i,j} = \frac{\alpha^{+}_{i-\frac{1}{2},j}\lambda_{i-1,j} - \alpha^{-}_{i+\frac{1}{2},j}\lambda_{i+1,j}}{\Delta q} + \frac{\beta^{+}_{i,j-\frac{1}{2}}\lambda_{i,j-1} - \beta^{-}_{i,j+\frac{1}{2}}\lambda_{i,j+1}}{\Delta r}. \tag{C-7}$$

This equation expresses $\lambda_{i,j}$ as a function of its neighboring values $\lambda_{i\pm1,j}$ and $\lambda_{i,j\pm1}$. Based on this local scheme, the fast-sweeping method can be used as a global scheme to solve this equation, which is similar to the one described in Leung and Qian (2006) to solve the adjoint-state equation for the isotropic case. In general, a single iteration is enough to converge. However, for a complex model with an irregular surface and heterogeneous velocity, rays are oscillating and more iterations are needed until λ converges.

REFERENCES

Aki, K., A. Christoffersson, and E. S. Husebye, 1977, Determination of the three-dimensional seismic structure of the lithosphere: Journal of Geophysical Research, **82**, 277–296, doi: 10.1029/JB082i002p00277.

Benaichouche, A., M. Noble, and A. Gesret, 2015, First arrival traveltime tomography using the fast marching and the adjoint state technique: 77th Annual International Conference and Exhibition, EAGE, 1–5, Extended Abstracts, doi: 10.3997/2214-4609.201412568.

Fomel, S., S. Luo, and H. Zhao, 2009, Fast sweeping method for the factored eikonal equation: Journal of Computational Physics, **228**, 6440–6455, doi: 10.1016/j.jcp.2009.05.029.

Guo, G., H. Lan, and L. Chen, 2019, A comparative study of both model expansion and topography flatten in topography handling in seismic traveltime tomography: Chinese Journal of Geophysics, **62**, 1704–1715.

Guo, X., R. Gao, L. Sanzhong, X. Xu, X. Huang, H. Wang, W. Li, S. Zhao, and X.-Y. Li, 2016, Lithospheric architecture and deformation of NE Tibet: New insights on the interplay of regional tectonic processes: Earth and Planetary Science Letters, **449**, 89–95, doi: 10.1016/j.epsl.2016.05.045.

Han, S., W. Zhang, and J. Zhang, 2017, Calculating qP-wave traveltimes in 2-D TTI media by high-order fast sweeping methods with a numerical quartic equation solver: Geophysical Journal International, **210**, 1560–1569, doi: 10.1093/gji/ggx236.

Hole, J. A., 1992, Nonlinear high-resolution three-dimensional seismic travel time tomography: Journal of Geophysical Research, Solid Earth, **97**, 6553–6562, doi: 10.1029/92JB00235.

Hole, J. A., R. D. Catchings, K. C. S. Clair, M. J. Rymer, D. A. Okaya, and B. J. Carney, 2001, Steep-dip seismic imaging of the shallow San Andreas Fault near Parkfield: Science, **294**, 1513–1515, doi: 10.1126/science.1065100.

Huang, G., S. Luo, J. Deng, and V. Vavryčuk, 2020, Traveltime calculations for qP-, qSV- and qSH- waves in two-dimensional tilted transversely isotropic media: Journal of Geophysical Research, Solid Earth, **125**, e2019JB018868, doi: 10.1029/2019JB018868.

Huang, J., and G. Bellefleur, 2011, Joint transmission and reflection traveltime tomography in imaging permafrost and thermokarst lakes in Northwest Territories, Canada: The Leading Edge, **30**, 1304–1312, doi: 10.1190/1.3663404.

Huang, J., and G. Bellefleur, 2012, Joint transmission and reflection traveltime tomography using the fast sweeping method and the adjoint-state technique: Geophysical Journal International, **188**, 570–582, doi: 10.1111/j.1365-246X.2011.05273.x.

Knapp, C. C., J. H. Knapp, and J. A. Connor, 2004, Crustal-scale structure of the South Caspian Basin revealed by deep seismic reflection profiling: Marine and Petroleum Geology, **21**, 1073–1081, doi: 10.1016/j.marpetgeo.2003.04.002.

Korenaga, J., W. S. Holbrook, G. M. Kent, P. B. Kelemen, R. S. Detrick, H. C. Larsen, J. R. Hopper, and T. Dahl-Jensen, 2000, Crustal structure of the Southeast Greenland margin from joint refraction and reflection seismic tomography: Journal of Geophysical Research, Solid Earth, **105**, 21591–21614, doi: 10.1029/2000JB900188.

Koulakov, I., 2009, LOTOS code for local earthquake tomographic inversion: Benchmarks for testing tomographic algorithms: Bulletin of the Seismological Society of America, **99**, 194–214, doi: 10.1785/0120080013.

Lan, H., and L. Chen, 2018, An upwind fast sweeping scheme for calculating seismic wave first-arrival travel times for models with an irregular free surface: Geophysical Prospecting, **66**, 327–341, doi: 10.1111/1365-2478.12513.

Lan, H., L. Chen, and J. Badal, 2018, A hybrid method for calculating seismic wave first-arrival traveltimes in two-dimensional models with an irregular surface: Journal of Applied Geophysics, **155**, 70–77, doi: 10.1016/j.jappgeo.2018.05.011.

Lan, H., and Z. Zhang, 2013a, A high-order fast-sweeping scheme for calculating first-arrival travel times with an irregular surface: Bulletin of the Seismological Society of America, **103**, 2070–2082, doi: 10.1785/0120120199.

Lan, H., and Z. Zhang, 2013b, Topography-dependent eikonal equation and its solver for calculating first-arrival traveltimes with an irregular surface: Geophysical Journal International, **193**, 1010–1026, doi: 10.1093/gji/ggt036.

Lelièvre, P. G., C. G. Farquharson, and C. A. Hurich, 2011, Inversion of first-arrival seismic traveltimes without rays, implemented on unstructured grids: Geophysical Journal International, **185**, 749–763, doi: 10.1111/j.1365-246X.2011.04964.x.

Leung, S., and J. Qian, 2006, An adjoint state method for three-dimensional transmission traveltime tomography using first-arrivals: Communications in Mathematical Sciences, **4**, 249–266, doi: 10.4310/CMS.2006.v4.n1.a10.

Li, Y., L. Dong, and Y. Liu, 2017, First-arrival traveltime tomographt based on a new preconditioned adjoint-state method: Chinese Journal of Geophysics, **60**, 3934–3941.

Liu, Y., L. Dong, Y. Wang, J. Zhu, and Z. Ma, 2009, Sensitivity kernels for seismic fresnel volume tomography: Geophysics, **74**, no. 5, U35–U46, doi: 10.1190/1.3169600.

Liu, Y., J. Teng, T. Xu, J. Badal, Q. Liu, and B. Zhou, 2017, Effects of conjugate gradient methods and step-length formulas on the multiscale full waveform inversion in time domain: Numerical experiments: Pure and Applied Geophysics, **174**, 1983–2006, doi: 10.1007/s00024-017-1512-3.

Luo, S., and J. Qian, 2012, Fast sweeping methods for factored anisotropic eikonal equations: Multiplicative and additive factors: Journal of Scientific Computing, **52**, 360–382, doi: 10.1007/s10915-011-9550-y.

Ma, T., and Z. Zhang, 2015, Topography-dependent eikonal traveltime tomography for upper crustal structure beneath an irregular surface: Pure and Applied Geophysics, **172**, 1511–1529, doi: 10.1007/s00024-014-0984-7.

Noble, M., P. Thierry, C. Taillandier, and H. Calandra, 2010, High-performance 3D first-arrival traveltime tomography: The Leading Edge, **29**, 86–93, doi: 10.1190/1.3284057.

Plessix, R. E., 2006, A review of the adjoint-state method for computing the gradient of a functional with geophysical applications: Geophysical Journal International, **167**, 495–503, doi: 10.1111/j.1365-246X.2006.02978.x.

Qian, J., Y. Zhang, and H. Zhao, 2007, A fast sweeping method for static convex Hamilton-Jacobi equations: Journal of Scientific Computing, **31**, 237–271, doi: 10.1007/s10915-006-9124-6.

Rajasekaran, S., and G. A. McMechan, 1995, Prestack processing of land data with complex topography: Geophysics, **60**, 1875–1886, doi: 10.1190/1.1443919.

Rawlinson, N., and B. L. N. Kennett, 2008, Teleseismic tomography of the upper mantle beneath the southern Lachlan Orogen, Australia: Physics of the Earth & Planetary Interiors, **167**, 84–97, doi: 10.1016/j.pepi.2008.02.007.

Rawlinson, N., S. Pozgay, and S. Fishwick, 2010, Seismic tomography: A window into deep earth: Physics of the Earth and Planetary Interiors, **178**, 101–135, doi: 10.1016/j.pepi.2009.10.002.

Rawlinson, N., and M. Sambridge, 2004, Wave front evolution in strongly heterogeneous layered media using the fast marching method: Geophysical Journal International, **156**, 631–647, doi: 10.1111/j.1365-246X.2004.02153.x.

Reshef, M., 1991, Depth migration from irregular surfaces with depth extrapolation methods: Geophysics, **56**, 119–122, doi: 10.1190/1.1442947.

Roecker, S., C. Thurber, K. Roberts, and L. Powell, 2006, Refining the image of the San Andreas Fault near Parkfield, California using a finite difference travel time computation technique: Tectonophysics, **426**, 189–205, doi: 10.1016/j.tecto.2006.02.026.

Salcedo, M., S. Garambois, P. Le Bouteiller, Y. Li, G. Sénéchal, C. Danquigny, and J. Virieux, 2020, Matrix-free crosshole elliptical-anisotropy tomography: Parametrization analysis and GPR applications in carbonates: Near Surface Geophysics, **18**, 697–712, doi: 10.1002/nsg.12116.

Sambolian, S., S. Operto, A. Ribodetti, B. Tavakoli, and J. Virieux, 2019, Parsimonious slope tomography based on eikonal solvers and the adjoint-state method: Geophysical Journal International, **218**, 456–478, doi: 10.1093/gji/ggz150.

Sei, A., and W. W. Symes, 1994, Gradient calculation of the travel time cost function without ray-tracing: 64th Annual International Meeting, SEG, Expanded Abstracts, 1351–1354, doi: 10.1190/1.1822780.

Sethian, J. A., and M. A. Popovici, 1999, Three dimensional traveltimes computation using the fast marching method: Geophysics, **64**, 516–523, doi: 10.1190/1.1444558.

Taillandier, C., M. Noble, H. Chauris, and H. Calandra, 2009, First-arrival traveltime tomography based on the adjoint-state method: Geophysics, **74**, no. 6, WCB1–WCB10, doi: 10.1190/1.3250266.

Tavakoli, F. B., 2017, Adjoint slope tomography: A velocity macro-model building tool for seismic imaging: Ph.D. thesis, Université Côte d'Azur.

Tavakoli, F. B., S. Operto, A. Ribodetti, and J. Virieux, 2017, Slope tomography based on eikonal solvers and the adjoint-state method: Geophysical Journal International, **209**, 1629–1647, doi: 10.1093/gji/ggx111.

Thurber, C., 1983, Earthquake locations and three-dimensional crustal structure in the Coyote Lake Area, central California: Journal of Geophysical Research, Solid Earth, **88**, 8226–8236, doi: 10.1029/JB088iB10p08226.

Vidale, J. E., 1988, Finite-difference calculation of travel times: Bulletin of the Seismological Society of America, **78**, 2062–2076.

Waheed, U. B., G. Flagg, and C. E. Yarman, 2016, First-arrival traveltime tomography for anisotropic media using the adjoint-state method: Geophysics, **81**, no. 4, R147–R155, doi: 10.1190/geo2015-0463.1.

Xu, T., G. Xu, E. Gao, Y. Li, X. Jiang, and K. Luo, 2006, Block modeling and segmentally iterative ray tracing in complex 3D media: Geophysics, **71**, no. 3, T41–T51, doi: 10.1190/1.2192948.

Ye, Z., R. Gao, Q. Li, H. Zhang, X. Shen, X. Liu, and C. Gong, 2015, Seismic evidence for the North China plate underthrusting beneath northeastern Tibet and its implications for plateau growth: Earth and Planetary Science Letters, **426**, 109–117, doi: 10.1016/j.epsl.2015.06.024.

Zhang, H., and C. Thurber, 2005, Adaptive mesh seismic tomography based on tetrahedral and Voronoi diagrams: Application to Parkfield, California: Journal of Geophysical Research, **110**, 225–243, doi: 10.1029/2004JB003186.

Zhang, J., U. S. ten Brink, and M. N. Toksöz, 1998, Nonlinear refraction and reflection travel time tomography: Journal of Geophysical Research, Solid Earth, **103**, 29743–29757, doi: 10.1029/98JB01981.

Zhang, X., Y. Wang, R. Gao, T. Xu, Z. Bai, X. Tian, and Q. Li, 2017, Vertical crustal motions across Eastern Tibet revealed by topography-dependent seismic tomography: Scientific Reports, **7**, 3243, doi: 10.1038/s41598-017-03578-z.

Zhang, Z., Z. Bai, S. Klemperer, X. Tian, T. Xu, Y. Chen, and J. Teng, 2013, Crustal structure across northeastern Tibet from wide-angle seismic profiling: Constraints on the Caledonian Qilian orogeny and its reactivation: Tectonophysics, **606**, 140–159, doi: 10.1016/j.tecto.2013.02.040.

Zhao, D., A. Hasegawa, and S. Horiuchi, 1992, Tomographic imaging of P and S wave velocity structure beneath northeastern Japan: Journal of Geophysical Research, Solid Earth, **97**, 19909–19928, doi: 10.1029/92JB00603.

Zhao, H., 2005, A fast sweeping method for eikonal equations: Mathematics of Computation, **74**, 603–627, doi: 10.1090/S0025-5718-04-01678-3.

Zhou, B., and S. Greenhalgh, 2008, Non-linear traveltime inversion for 3-D seismic tomography in strongly anisotropic media: Geophysical Journal International, **172**, 383–394, doi: 10.1111/j.1365-246X.2007.03649.x.

Zhou, B., X. Liang, G. Lin, X. Tian, G. Zhu, J. Mechie, and J. Teng, 2019, Upper crustal weak zone in central Tibet: An implication from three-dimensional seismic velocity and attenuation tomography results: Journal of Geophysical Research, Solid Earth, **124**, 4654–4672, doi: 10.1029/2018JB016653.

Zhou, X., H. Lan, L. Chen, and G. Guo, 2020, The factored eikonal equation in curvilinear coordinate system and its numerical solution: Chinese Journal of Geophysics, **63**, 638–651.

Zhou, X., H. Lan, L. Chen, G. Guo, Y. Lei, U. B. Waheed, and S. Pan, 2021, An iterative factored topography-dependent eikonal solver for anisotropic media: Geophysics, **86**, no. 5, U121–U134, doi: 10.1190/geo2020-0662.1.

Biographies and photographs of the authors are not available.